

Constraining accuracy of pairwise velocities using scale-free models

Sara Maleubre,^{1,2*} Daniel J. Eisenstein,³ Lehman H. Garrison,^{4,5} and Michael Joyce¹

¹ *Laboratoire de Physique Nucléaire et de Hautes Énergies, UPMC IN2P3 CNRS UMR 7585, Sorbonne Université, 4, place Jussieu, 75252 Paris Cedex 05, France*

² *Max Planck Institute for Extraterrestrial Physics, Giessenbachstrasse 1, 85748 Garching, Germany*

³ *Center for Astrophysics | Harvard & Smithsonian, 60 Garden St, Cambridge, MA 02138*

⁴ *Center for Computational Astrophysics, Flatiron Institute, 162 Fifth Ave., New York, NY 10010*

⁵ *Scientific Computing Core, Flatiron Institute, 162 Fifth Ave., New York, NY 10010*

Accepted XXX. Received YYY; in original form ZZZ

ABSTRACT

We present a continuation of an analysis that aims to quantify resolution of N -body simulations by exploiting large (up to $N = 4096^3$) simulations of scale-free cosmologies run using ABACUS. Here we focus on pairwise velocities of the matter field and of halo centres selected with both the ROCKSTAR and COMPASO algorithms. For the matter field, we find that convergence at the 1% level of the mean relative pairwise velocity can be demonstrated over a range of scales, evolving from a few times the grid spacing at early times to slightly below this scale at late times. Down to scales of order the force smoothing, convergence is obtained at $\sim 5\%$ precision, and shows a behaviour indicating asymptotic stable clustering. We also infer for LCDM simulations conservative estimates on the evolution of the lower cut-off to resolution (at 1% and 5% precision) as a function of redshift. For the halos, we establish convergence, for both ROCKSTAR and COMPASO, of mass functions at the 1% precision level and of the mean pair-wise velocities (and also 2PCF) at the 2% level. We find that of the two halo finders, ROCKSTAR exhibits greater self-similarity, specially on small scales and small masses. We also give resolution limits expressed as a minimum particle number per halo in a form that can be directly extrapolated to LCDM.

Key words: cosmology: large-scale structure of the Universe – methods: numerical

1 INTRODUCTION

Observational tests such as Type Ia supernovae (Perlmutter et al. 1997; Riess et al. 1998), large-scale structure analysis from Baryon Acoustic Oscillations (BAO, Eisenstein et al. 2005; Cole et al. 2005) and the temperature anisotropies of the cosmic microwave background (CMB, Jaffe et al. 2001; Pryke et al. 2002; Planck Collaboration et al. 2014) provide compelling evidence that the Universe is in an accelerated expansion. To explain this within the framework of General Relativity requires a new type of “dark” energy that accounts for about 70% of the total, and whose nature is still unknown. In the current standard model of cosmology (LCDM), this energy component is in the form of a cosmological constant. Alternative theoretical approaches either add extra degrees of freedom to characterize the energy content of the Universe or modify the Einstein-Hilbert action (for a review on these models see Clifton et al. 2012).

Ongoing and future surveys such as the Dark Energy Spectroscopic Survey (DESI) (DESI Collaboration et al. 2016) or the space-based mission *Euclid* (Laureijs et al. 2011) will provide large scale structure maps of the Universe of unprecedented statistical precision, allowing astronomers to measure the expansion history of the Universe and the growth rate of cosmic structures in sufficient detail to potentially distinguish between the different possible aforementioned scenarios.

Indeed, one of the most valuable tests to discriminate between

these multiple models observationally, and ultimately determine which can explain current data, consists in the study of the rate at which cosmic structures grow (see e.g. Perenon et al. 2019; Brando et al. 2021), as different theories can predict quite different growth histories even for the same background evolution. A popular way of constraining this growth rate is by analysing the corrections to galaxy redshifts due to their peculiar velocities, which produces a modification of galaxy clustering, an effect called redshift-space distortions (RSD, Jackson 1972; Kaiser 1987). Since peculiar velocities are caused by gravitational pull, we can trace a relation between the velocity field and the mass density field and thus estimate the rate at which structures grow.

In order to exploit this information, it is essential to calculate accurate theoretical predictions for the large-scale structure of the Universe. Below scales where the perturbative approaches break down, such calculations rely entirely on cosmological simulations performed using the N -body method. This approach approximates the continuous phase-space distribution of dark matter by that of a sparse finite sample of particles, and evolves them in a finite box with periodic boundary conditions. In this context, an important question is the accuracy and scale-range limitations of this method in attaining the physical limit.

The assessment of the accuracy to which results converge to values independent of the numerical parameters (time stepping, force accuracy parameters) introduced in the resolution of the N -body system is straightforward. In this respect, extensive code compar-

* E-mail: sara.maleubre@lphne.in2p3.fr

isons (Heitmann et al. 2008; Schneider et al. 2016; Garrison et al. 2019; Grove et al. 2022) give considerable added confidence in the precision of results for different statistics. Such comparisons do not address, however, the question of the accuracy with which these simulations represent the physical limit. While dependence on box size can be assessed by direct extrapolation studies (see e.g. Euclid Collaboration et al. 2019), assessing the accuracy limitations imposed at *small scales* due to the discretization of the matter field is much more complex. The reason is that there are, at least, two relevant unphysical parameters, the mean interparticle spacing (denoted Λ here) and the gravitational force smoothing (denoted ϵ), and numerical extrapolation to the continuum physical limit, corresponding to $\epsilon/\Lambda \rightarrow 0$, is in practice unattainable. Precise quantitative conclusions regarding it have remained elusive and sometimes controversial (see Joyce et al. 2021, for a discussion and some references).

Previous studies using N -body simulations have already used the information contain in the dark matter and halo pairwise velocity field to study plausible deviations from the standard model (Hellwing et al. 2014; Gronke et al. 2015; Bibiano & Croton 2017; Valogiannis et al. 2020). Such conclusions ultimately rely on the ability of the N -body method to accurately predict and compute the desired statistic and that of the chosen halo finder retrieving halo properties accurately. But halos are not uniquely defined entities, and their properties depend strongly on the algorithm adopted for their extraction. In addition to the aforementioned efforts in examining precision in N -body simulations, several studies have been carried out to assess the accuracy and resolution of different codes for halo recovery (see Knebe et al. 2011, for a review).

In this article, we use the techniques introduced in Joyce et al. (2021) and developed and applied also in Leroy et al. (2021); Garrison et al. (2021a); Garrison et al. (2021c) and Maleubre et al. (2022) to derive resolution limits arising from particle discretization for different statistics by analysing deviations from self-similarity in scale-free cosmological models. Here, we employ these methods to assess and quantify the limits arising from discretization on the precision at which the radial component of the pairwise velocity of the full dark matter field, and of halos, can be retrieved from N -body simulations. In addition, we revisit and develop further the analysis in Leroy et al. (2021) of the mass functions and two-point correlation function of halos, extending it to include both larger simulations and scale-free models with different exponents as well as to the new halo finder COMPASO (Hadzhiyska et al. 2022; Bose et al. 2022).

This article is structured as follows. The first part of the next section describes what scale-free cosmologies are and how their self-similar evolution can be used to determine the accuracy at which different statistics can be measured in N -body simulations. Next, we recall the expressions for the radial component of the pairwise velocity and the pair conservation equation, as well as give the equation for the latter in the context of scale-free cosmologies. We end the section with a description of the halo statistics that will be analysed. Section 3 contains a summary of the simulations used, as well as a brief description of ABACUS, the N -body code used for their computation. It also contains a description of the method used to estimate convergence of the different statistics in both the dark matter field and halos, and ends with a summary of the halo finders we compare (ROCKSTAR and COMPASO). In section 4 we present and analyse our results for both dark matter and halos, as well as infer resolution limits to non-scale-free cosmologies. Finally, we summarize our results in Section 5.

2 SCALE-FREE SIMULATIONS AND PAIRWISE VELOCITY

2.1 Scale-free simulations and Self Similarity

Scale-free cosmologies have an Einstein-de Sitter, EdS, ($\Omega_M = 1$) background and a power-law power spectrum ($P_k \propto k^n$) of initial perturbations, which are thus characterized by just one length scale, the scale of non-linearity. This can be defined by

$$\sigma_{\text{lin}}^2(R_{\text{NL}}, a) = 1 \quad (1)$$

where σ_{lin}^2 is the variance of normalized linear mass fluctuations in a sphere. Its temporal evolution can be calculated from linear perturbation theory as

$$R_{\text{NL}} \propto a^{\frac{2}{3+n}} \quad (2)$$

One can infer that, if the evolution of gravitational clustering is independent of any other length scale (notably ultraviolet or infrared cut-offs to the assumed power-law fluctuations), it must be *self-similar*, i.e., the temporal evolution of the statistics describing clustering is given by a spatial rescaling following Eq. 2. More specifically, any dimensionless function $F(x_1, x_2, \dots; a)$ describing clustering (where the x_i are the parameters on which the statistic depends) will obey a relation of the form

$$F(x_1, x_2, \dots; a) = F_0(x_i/X_{\text{NL},i}(a)) \quad (3)$$

where $X_{\text{NL},i}$ encodes the temporal dependence of the characteristic scale with the same dimensions as x_i (as inferred from R_{NL}).

Our interest in self-similarity is driven by the fact that it greatly simplifies the description of clustering: its time dependence is effectively trivial, and any statistic describing clustering is specified by the single time-independent function on the right-hand side of Eq. 3. As discussed in our previous papers, we can use this property to determine the range of scales that a simulation can reliably reproduce: any deviation from self-similarity arises necessarily from dependence on the *unphysical scales* proper to the N -body simulations.

2.2 Pairwise Velocity and pair-conservation equation

In this study we focus on the radial component of the mean pairwise velocity defined by

$$v_{12}^r = \left\langle (\mathbf{v}_1 - \mathbf{v}_2) \cdot \frac{\mathbf{r}}{|\mathbf{r}|} \right\rangle \quad (4)$$

where the velocity difference ($\mathbf{v}_1 - \mathbf{v}_2$) of a pair of objects is projected on to their separation vector \mathbf{r} , and $\langle \dots \rangle$ denotes the ensemble average. It can be estimated in a finite simulation by directly averaging the pair velocity over all pairs. To do so, here we have coded an appropriate modification of the analysis tool *Corrfunc* (Sinha & Garrison 2019, 2020). To facilitate our analysis based on self-similarity, we will always consider below the dimensionless ratio of v_{12}^r to the Hubble flow (Hr), so that self-similarity has the simple expression in the form of Eq. 3.

The first half of this paper focuses on the matter field, and the choice to study v_{12}^r is motivated by the fact that, in this case, it can also be related to the two-point correlations of mass density via the so-called pair conservation equation. This relation was first derived by Davis & Peebles (1977) as a consequence of the BBGKY equations. In their statistical description, matter was approximated by a set of identical particles of mass m , making their theoretical results directly applicable to those of N -body simulations. Starting

from the continuity equation for the density contrast (zeroth moment of the Vlasov equation) one obtains the pair conservation equation:

$$\frac{\partial \xi_{12}}{\partial \tau} + \nabla_{12} \cdot [\mathbf{v}_{12}^r (1 + \xi_{12})] = 0 \quad (5)$$

where τ is equal to the conformal time and ξ_{12} is the standard reduced two-point density-density correlation function (2PCF) defined as the ensemble average at two different locations $(1 + \xi_{12} = \langle (1 + \delta(\mathbf{x}_1))(1 + \delta(\mathbf{x}_2)) \rangle)$.

This can be conveniently rewritten as (Nityananda & Padmanabhan 1994):

$$\frac{v_r}{Hr} = -\frac{1}{3(1 + \xi)} \frac{\partial \bar{\xi}}{\partial \ln a} \quad (6)$$

where $\bar{\xi} = 3x^{-3} \int_0^x \xi y^2 dy$, the cumulative two-point correlation function (cumulative 2PCF), is the average 2PCF interior to x where we have normalized the velocity to the Hubble flow (Hr). For economy, we have dropped the indices 12 in the two-point quantities. As Eq. 6 is exact, it implies that we can estimate v_r in a finite sample indirectly, using instead of the velocities themselves the direct estimators of the 2PCF, the cumulative 2PCF and its derivative, combined in the appropriate way. This has been previously exploited in an early study of the pair velocity in scale-free models by Jain (1997) focused on the question of whether clustering become *stable* at small scales (Peebles 1974), i.e. whether it tends to become stationary in physical coordinates, corresponding to $v_r = -Hr$.

In the context of scale-free models and their expected self-similarity, it is convenient to rewrite Eq. 6 with the time derivative taken at a fixed value of the rescaled comoving separation (i.e. at fixed r/R_{NL} rather than fixed r)

$$\frac{v_r}{Hr} = -\frac{2}{3+n} \left(\frac{\bar{\xi}}{\xi} - 1 \right) \frac{\xi}{1 + \xi} - \frac{1}{3(1 + \xi)} \frac{\partial \bar{\xi}}{\partial \ln a} \Big|_{r/R_{\text{NL}}} \quad (7)$$

When the two-point density correlations (as described by ξ and $\bar{\xi}$) are self-similar, the last term vanishes and we can infer that v_r is also self-similar. On the other hand, self-similarity of ξ and $\bar{\xi}$ is not a requirement for that of v_r . We will pay careful attention to this point in our analysis below, and we will show that there is in fact a regime in our simulations in which v_r approximates well self-similarity while the 2PCF does not.

2.3 Halo quantities

In Sec. 4.2 we will use self-similarity to test different halo selection algorithms. As for the matter field, our focus is on the convergence and accuracy of the measurements obtained from these algorithms of the mean pairwise velocity of halo centres. As the latter are measured as a function of halo mass, we will start by analysing the convergence of the mass function (HMF) as a function of mass, extending a similar analysis already given in Leroy et al. (2021) to incorporate the CompaSO algorithm (and also the results of larger simulations and scale-free models).

We recall that the halo mass function is just the number density of halos of a given mass at a given redshift. Following the treatment of Press & Schechter Press & Schechter (1974), it is convenient to express it in terms of the ‘‘multiplicity’’ function f (Jenkins et al. 2001; Tinker et al. 2008) defined by

$$\frac{dn}{d \ln M} = f(\sigma) \frac{\bar{\rho}}{M} \frac{d \ln \sigma^{-1}}{d \ln M} \quad (8)$$

where $\bar{\rho}$ is the mean matter density, and σ is defined by Eq. 1 but now as a function of mass using $M_{\text{NL}} \propto R_{\text{NL}}^3$.

For scale-free cosmologies, we can conveniently express $f(\sigma)$ in terms of the rescaled mass M/M_{NL} as

$$f(M/M_{\text{NL}}) = \frac{6}{3+n} \frac{M^{2n}}{\bar{\rho}} \quad (9)$$

where we used $n \equiv dn/dM$ and from Eq. 1 $d \ln \sigma^{-1}/d \ln M = (3+n)/6$

The halo-halo 2PCF, $\xi_{\text{hh}}(r, M, a)$, is a dimensionless function of the separation r and of the halo mass M , calculated at a given snapshot. Similarly, the radial component of the pairwise velocity can be computed as the correlation between two centres weighted by their projected velocity. In both cases, if self-similarity applies, it is conveniently rewritten in terms of the dimensionless rescaled functions

$$\xi_{\text{hh}}(r, M, a) = \xi_{\text{hh},0}(r/R_{\text{NL}}, M/M_{\text{NL}}) \quad (10)$$

$$\frac{v_{r,\text{hh}}}{Hr} = V_{r,0}(r/R_{\text{NL}}, M/M_{\text{NL}}). \quad (11)$$

3 NUMERICAL SIMULATIONS

3.1 ABACUS code and simulation parameters

We report results based on the simulations listed in Table 1, performed using the ABACUS N -body code (Garrison et al. 2021b). ABACUS offers high performance and accuracy, based on a high-order multiple method to solve far-field forces and an accelerated GPU calculation of near-field forces by pairwise evaluation. While the $N = 1024^3$ simulations were run using local facilities at the Harvard-Smithsonian Center for Astrophysics (CfA), the larger $N = 4096^3$ simulation are part of the ABACUSUMMIT project (Maksimova et al. 2021), which used the Summit supercomputer of the Oak Ridge Leadership Computing Facility.

The simulation data we exploit in this article are summarized in Table 1. As in Maleubre et al. (2022), we have simulated three different exponents ($n = -1.5$, $n = -2.0$ and $n = -2.25$), chosen to probe the range relevant to standard (i.e. LCDM-like) models. For the first two exponents, we have two simulations with different N but otherwise identical parameters, allowing us to study finite box size effects. For the larger ($N = 4096^3$) simulations, the statistics have been calculated on (random) sub-samples of different sizes (25%, 3%) to facilitate the assessment of finite sampling effects. For the other two spectral indices, $n = -2.0$ and $n = -2.25$, we have four $N = 1024^3$ simulations, each with identical N -body parameters but different realizations of the IC. These will be analysed below, both individually and as an average.

We work in units of the mean inter-particle (i.e. initial grid) spacing, $\Lambda = L/N^{1/3}$. The essential time-stepping parameter in ABACUS has been chosen as $\eta = 0.15$ for all simulations, and the additional numerical parameters have been set as detailed in Maleubre et al. (2022). These choices are based on the extensive convergence tests of these parameters reported in our previous studies (see Joyce et al. 2021; Garrison et al. 2021a).

The remaining parameter correspond to the softening length. As previously introduced in Garrison et al. (2016), ABACUS performs a spline softening derived as a Taylor expansion in r of the Plummer softening expression, requiring a smooth transition at the softening scale up to the second derivative. All softening lengths in this study have been fixed in proper coordinates for the interesting redshifts, decreasing as $\epsilon(a) \propto 1/a$ in comoving coordinates, those used by the simulation. To avoid a too large softening at earlier times,

we fixed it in comoving coordinates down to a_0 , the first output of our simulation, and change to proper from then on. For all the simulations studied here, we use $\epsilon(a_0)/\Lambda = 0.3$. This value has been chosen following the results in [Garrison et al. \(2021a\)](#) and [Maleubre et al. \(2022\)](#), being both accurate and efficient for the spectral indices analysed.

The start of the simulation ($a = a_i$) is chosen so that top-hat density fluctuations at the particle spacing are given by

$$\sigma_i(\Lambda, a_i) = 0.03 \quad (12)$$

While the first output epoch ($a = a_0$) corresponds approximately to the formation of the first non-linear structures, fixed at the time at which fluctuations of peak-height $\nu \approx 3$ are expected to virialize in the spherical collapse model ($\sigma \sim \delta_c/\nu$, with $\delta_c = 1.68$):

$$\sigma_0(\Lambda, a_0) = 0.56 \quad (13)$$

Subsequent output values are spaced by a factor $\sqrt{2}$ in the non-linear mass scale. Given that $M_{\text{NL}} \propto R_{\text{NL}}^3$ and substituting in Eq. 13, we get:

$$\Delta \log_2 a = \frac{3+n}{6} \Delta \log_2 M_{\text{NL}} = \frac{3+n}{12} \quad (14)$$

We use $\log_2(a/a_0)$, as the time variable of our analysis, which indicates how many epochs have passed since the first output. It is also convenient to define the variable

$$S = \frac{12}{3+n} \log_2 \left(\frac{a_S}{a_0} \right) \quad (15)$$

with $S = 0, 1, 2, \dots$ corresponding to the different outputs of the simulation.

Initial conditions have been set up using a modification to the standard Zel'dovich approximation (ZA), detailed in [Garrison et al. \(2016\)](#). This includes a second order lagrangian perturbation theory (2LPT) correction as well as particle linear theory (PLT) corrections as described in [Joyce & Marcos \(2007\)](#) and [Garrison et al. \(2016\)](#). The latter corrects the initial conditions for discreteness effects at early times, so that the result of fluid evolution is reproduced at a target time $a = a_{\text{PLT}}$. For all our simulations here we have $a_{\text{PLT}} = a_0$, with a_0 defined by Eq. 13.

3.2 Estimation of converged values

As in our previous papers, we will assess the convergence to the physical limit by studying the temporal evolution of statistics, which become time-independent in the case of self-similarity. To make this study quantitative — i.e. to identify estimated converged values, and converged regions at some precision — we need to adopt appropriate criteria. While the conclusions drawn should not of course depend significantly on the chosen criteria, these criteria are intrinsically somewhat arbitrary in detail. In practice, their choice is made based on visual examination of data. We follow here the simple procedure described in [Maleubre et al. \(2022\)](#). It allows us to estimate a converged value and converged region at a chosen precision, per rescaled bin for each of the statistics analysed in this paper. The method is equivalent for all our dimensionless statistics, whether they are matter-field ($\xi, \bar{\xi}, v_r/Hr$) or halo ($f(M/M_{\text{NL}}), \xi_{\text{hh}}, v_{r,\text{hh}}/Hr$). We denote our chosen statistic by X in the following.

We first calculate an estimated converged value (denoted as X_{est}) in each rescaled bin as the average of the statistic in a specific temporal window. The width of this window is conveniently specified by a number of snapshots w , corresponding to an increase in the non-linearity scale by a factor of $2^{w/6}$ (below we use $w = 5$). To identify

the location of the candidate converged window, we “slide” a window of width w across the data to find that which minimizes

$$\Delta = \frac{|X_{\text{max}} - X_{\text{min}}|}{2\mu_X} \quad (16)$$

where X_{max} , X_{min} , and μ_X are respectively the maximum, minimum, and average values in the window. Specifying now a parameter p characterizing the precision of convergence, any bin is considered to be converged only if the minimal value of Δ is less than p .

To identify the region of convergence to this estimated value (at precision p), for each rescaled bin with a converged X_{est} , we find the largest (containing at least three consecutive snapshots, though again this number is not essential) connected temporal window verifying

$$\frac{|X - X_{\text{est}}|}{X_{\text{est}}} < p. \quad (17)$$

We denote X_{conv} the average calculated over this new window, and take this as the estimated converged value of the statistic for the given rescaled bin. We note that, in the following (as in [Maleubre et al. 2022](#)), when we say that we have precision at $x\%$ we mean that $p = x/100$ ¹.

In the results presented below, all two-point quantities have been calculated over the same r/R_{NL} grid, whether they are matter-field or halo. We use bins of constant logarithmic spacing $1 + (\Delta r/r) \approx 2^{1/12}$ ([Maleubre et al. 2022](#), following), ensuring that bins of different snapshots match when rescaled by R_{NL} to facilitate comparison between them. In order to reduce statistical noise sufficiently, we have rebinned by grouping four such bins, corresponding to $\Delta r/r \approx 0.26$. In the case of the HMF, mass-bins were chosen and rebinned so that $\Delta m/m \approx 0.5$. In our presentation below we label our bins, for simplicity, just by the value of the rescaled variable at the geometrical centre of the bin.

3.3 Halo Finders: ROCKSTAR and COMPASO

In this paper we analyse results from two different group-finding algorithms, comparing their level of resolution in a set of halo-statistics, as well as the accuracy of convergence. Competitive assignment to spherical overdensities (COMPASO) ([Hadzhiyska et al. 2022](#)) is a newly developed halo-finder specifically created to meet the demanding requirements of the ABACUS SUMMIT cosmological N -body simulations. It runs on-the-fly, as part of the simulation code itself, with two of its primary requirements being keeping up with the high speed of ABACUS ([Maksimova et al. 2021](#)), and support the creation of merger trees to be used in the Dark Energy Spectroscopic Instrument (DESI) project. On the other hand, Robust Overdensity Calculation using K-Space Topologically Adaptive Refinement (ROCKSTAR) ([Behroozi et al. 2013](#)) is a well established, widely used halo-finding algorithm. It has been subjected previously to self-similarity tests (for the HMF and 2PCF) in scale-free cosmologies in ([Leroy et al. 2021](#)). In Sec. 4.2 we will compare results from both group-finder algorithms.

The COMPASO algorithm is a configuration-space, FoF and SO algorithm to compute halos from N -body simulations. It first obtains a measurement of the local density using a kernel of the form $W = 1 - r^2/b_{\text{kernel}}^2$, where typically $b_{\text{kernel}} = 0.4\Lambda$. Particles with a density Δ higher than a chosen threshold are then grouped together into FoF groups (L0 halos). The main halos (L1 halos) are then formed inside these groups. Within each group, the algorithm finds

¹ What we denote p here corresponds to $\alpha/2$ in [Maleubre et al. \(2022\)](#).

Table 1. Summary of the N -body simulation data used for the analysis of this paper. The first column shows the spectral index of the initial PS, N is the number of particles of each simulation, and the third column shows the number of simulations with identical parameters but different realizations of the IC. The fourth column shows the available statistic and sampling of the matter field, while the last one indicates the run Halo Finder.

n	N	num. sims.	DM Statistic (%)	Halo Finder
$n = -1.5$	4096^3	1	v_r and ξ (25%)	COMPASO
$n = -1.5$	1024^3	1	v_r and ξ (100%)	ROCKSTAR
$n = -2.0$	4096^3	1	ξ (3%)	COMPASO
$n = -2.0$	1024^3	4	v_r and ξ (100%)	ROCKSTAR
$n = -2.25$	1024^3	4	v_r and ξ (100%)	–

the particle with the highest kernel density—the first halo nucleus—and makes a preliminary assignment to it of all particles within a radius R_{L1} (innermost radius enclosing $\Delta < \Delta_{L1} = 200$ in EdS). Particles outside $80\% \text{ of } R_{L1}$ are eligible to become their own halo centre as long as they are the densest within their kernel radius. The algorithm then finds the next highest density among eligible particles, which becomes the next halo nucleus. Particles are assigned to this nucleus as the first, but if a particle belongs to both halos one and two, the algorithm performs a competitive assignment. This reassigns a particle to a new halo if its enclosed density with respect to the new halo is twice that of the old one. The search for new halo centres within $L0$ continues until no particles remain that are likely to nucleate halos of sufficient density.

COMPASO can sometimes fragment elongated halos into multiple objects, due to its spherical nature, or identify substructure as a distinct halo at one epoch that was already identified as a monolithic halo at a previous epoch. For this reason, a cleaning procedure is performed in post-processing, relying on merger-trees information (Bose et al. 2022). This procedure checks what fraction of the particles of a halo at time t_i come from a much larger halo located at a similar position at time t_{i-1} and t_{i-2} . If a sufficiently large fraction did, then the newer halo is deemed a “potential split” and merged into the larger halo. In addition, if at an earlier redshift a halo peak mass exceeds more than twice its present day mass, it is also merged into a more massive neighbour, from whom it had presumably split off. The described cleaning method affects, in general, low-mass halos around more massive ones, appending their particle list to the latter, and resulting in cleaned halo catalogues with a lower number of smaller halos vs. a larger number of bigger halos. As we will show in Sec. 4.2.1, this shifts the value of the HMF in each mass-bin exactly in the correct direction to preserve self-similarity, which is evidence for the good performance of the procedure.

ROCKSTAR is a six phase-space dimensions plus time halo finder, aiming at maximizing consistency of halo properties across snapshots. The code starts by creating FoF groups of a linking length larger than standard ($b = 0.28$ by default), which assures that virial spherical overdensities can be determined within. For each of these FoF groups, a phase-space metric is defined by normalizing the positions and velocities of the particles by the position and velocity dispersions of the group, such that for two particles p_1 and p_2 the distance metric is defined by:

$$d(p_1, p_2) = \left(\frac{|\mathbf{x}_1 - \mathbf{x}_2|^2}{\sigma_x^2} + \frac{|\mathbf{v}_1 - \mathbf{v}_2|^2}{\sigma_v^2} \right)^{1/2} \quad (18)$$

The algorithm now performs a modified FoF in phase-space within each group, where it links particles with an adaptive phase-space linking length such that a constant fraction of particles (default 70%) is always linked together with at least another particle into subgroups.

The process repeats for each subgroup, creating a hierarchical set of structures until a minimum size substructure is found at the deepest level. Seed halos are placed at this final structure, and particles at higher levels are assigned to the closest seed halo in phase-space, where now the metric (Eq. 18) is calculated with respect to the seed halo. More than one seed can be found within each of the first level FoF groups, corresponding to either a halo or subhalo. This categorization is performed by including temporal information of previous steps, following particle-halo associations across time-steps. During its final step, ROCKSTAR calculates the gravitational potential of all particles using a modified Barnes-Hut method in order to unbind particles.

ROCKSTAR defines halo masses by using various (user-specified) SO criteria. Following the results in Leroy et al. (2021), we restrict ourselves in this study to using the SO mass corresponding to the virial radius, including all halo structures and considering only gravitationally bound mass (STRICT_SO_MASSES=0). Finally, halo centres and velocities are calculated in the code using a subset of the innermost particles ($\sim 10\%$ of the halo radius), minimizing a Poisson error σ/\sqrt{N} .

ROCKSTAR has been run with *default* parameters but for MIN_HALO_OUTPUT_SIZE=25 and TEMPORAL_HALO_FINDING = 0, to be consistent with (Leroy et al. 2021)

4 RESULTS

4.1 Radial pairwise velocity of matter field

As discussed above, in a scale-free cosmology, self-similarity implies an independence of the results of an N -body simulation of their discretization parameters. By carefully examining the departures from self-similarity that are actually measured, we can infer how the resolved scales depend on the unphysical scales in the N -body simulation. We report in this section this analysis for the mean pairwise velocity in the matter field.

4.1.1 Direct estimation

As discussed in subsection 2.2, v_r/Hr can be estimated directly from the measured particle velocities, or indirectly from measurements of the 2PCF. We consider first the former estimate. Fig. 1 shows the estimated v_r/Hr as a function of time (parameterized by the variable $\log_2(a/a_0)$) at different rescaled distance, for spectral indices $n = -1.5$, $n = -2.0$ and -2.25 . Each plot correspond to the simulations with the highest number of particles ($N = 4096^3$ for $n = -1.5$, and the average of the four $N = 1024^3$ simulations for the other). The left panel gives v_r/Hr as a function of r/Λ (with Λ the grid spacing), while the right panel gives it as a function of the rescaled variable

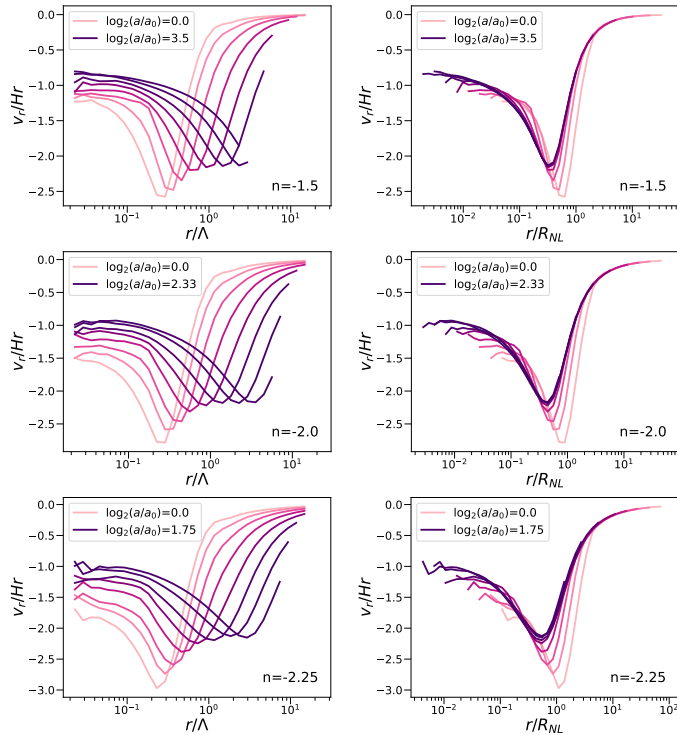


Figure 1. Directly estimated v_r/Hr as a function of comoving separation (left column) and of the rescaled coordinate r/R_{NL} (right column), for simulations with spectral indices $n = -1.5$, $n = -2.0$ and $n = -2.25$ ($N = 4096^3$ for the former exponent and average over four $N = 1024^3$ for the last two). Self-similar evolution corresponds to a superposition of the curves in the rescaled plots. The times shown correspond to every fourth snapshot $S = 0, 4, 8, \dots$ (where S is as defined in Eq. 15) over the total time-span of the simulations.

r/R_{NL} . Self-similarity corresponds to the superposition of the data at different times in the latter plot.

These plots show qualitatively the general behaviour of the statistic, which is similar to that seen for the 2PCF (Joyce et al. 2021) and the PS (Maleubre et al. 2022). Self-similarity can be seen to propagate from larger comoving scales, significantly above Λ at early times, to smaller scales as time evolves. In particular, the scales around the “turnaround” point — corresponding to the maximal radial infall velocity — are only resolved at later times. As for the 2PCF and PS in our previous studies, the redder the index, the more reduced is the range of approximate self-similarity. This is a reflection primarily of the smaller range of scale-factor which is accessible in simulations of a fixed size as n decreases, and also, as we will see further below, of larger finite box size effects. Finally, we note that all three models appear to show the same behaviour at asymptotically small scales, tending to a value close to -1 , the value predicted by the stable clustering hypothesis. We will assess these behaviours quantitatively below in subsection 4.1.3.

4.1.2 Estimation using pair conservation

We next consider the estimation of v_r from the estimated 2PCF, using the exact relation Eq. 7 for v_r in terms of ξ , $\dot{\xi}$ and $\ddot{\xi}$. As noted, we can also test the validity of the relation when the term in $\ddot{\xi}$ vanishes, which corresponds to self-similarity of $\dot{\xi}$. Fig. 2 shows the normalized pairwise velocity at each rescaled coordinate for a set of selected redshifts, in the same way as in the right panel of Fig. 1. In

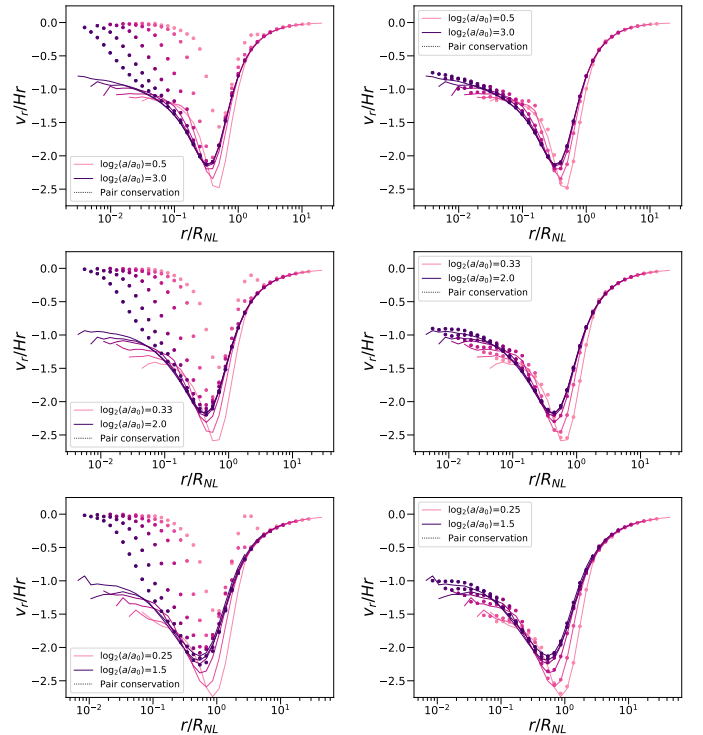


Figure 2. Comparison of different estimators of v_r/Hr as a function of the rescaled length r/R_{NL} , for the same simulations as in Fig. 1. The solid lines in each pair of panels (left and right) are identical and correspond to the results obtained by direct estimation using the velocities (as in Fig. 1). The dots correspond, in the left panels, to estimations using pair-counting and the assumption of self-similarity of the 2-pt statistics i.e. using Eq. 7 with the last term set to zero. In the right panels, this last term is also included in the estimator.

addition, we have added a dotted line which gives the new estimation obtained using pair conservation. The left panel excludes the non-self-similar term, while the right panel corresponds to the full (exact) expression Eq. 7. To estimate the time derivative, we have simply used a finite difference estimate on the closest two “neighbouring” snapshots.

In the right panels we see that, as required by pair conservation, we recover v_r to a very good approximation from the alternative estimator. The very small differences can be attributed to finite particle number noise and possible systematic offset due to the estimation of the time derivative. Given the close spacing (Eq. 14) of our snapshots, it is unsurprising that any such effect appears to be small. At small scales, on the other hand, close examination shows that the pair conservation estimator is slightly less noisy than the direct one. This is as might be anticipated: because of the intrinsic dispersion in the pairwise velocities, we can expect its average to have a greater variance than the direct pair count (as noted previously by Jain 1997). Thus, in assessing what is required to obtain an accurate estimation of the pairwise velocity, one needs to consider between the need to have closely spaced outputs to accurately estimate the time derivative if pair counting is used, or a larger volume for accurate direct estimation.

The left panels, on the other hand, show very large discrepancies between the two estimators, which we can infer as being due to a significant deviation in the corresponding range of the (integrated) 2PCF from self-similarity. Indeed, we can see that this is the case from the corresponding direct analysis of $\dot{\xi}$ displayed in Fig. 3: the

scales at which the agreement of the estimators break corresponds to the break from self-similarity of $\bar{\xi}$. We note that, at late times, the associated break appears to occur at a scale where v_r/Hr approaches -1 , the value corresponding to stable clustering. Thus, there is indeed a range where approximate self-similarity appears to persist despite the fact that the 2PCF differ much more from their physical values, and this range appears to correspond, at later times, to that where stable clustering is well approximated.

4.1.3 Quantitative determination of resolved scales

To better understand, and then also quantify, the limitations on the range of self-similarity arising from the different unphysical simulation parameters (specifically Λ , ϵ and N) we now study more closely the evolution as a function of time of v_r/Hr (estimated directly and indirectly via pair conservation), and of ξ and $\bar{\xi}$, for fixed values of r/R_{NL} . This corresponds to taking the values on vertical lines in the right panels of Fig. 1 (and the equivalent plots for ξ and $\bar{\xi}$). As discussed, self-similarity of the statistic then corresponds to time independence, i.e. to convergence (in some range) of the time series to a fixed value.

Fig. 4 and 5, for spectral indices $n = -1.5$ and $n = -2.0$ respectively, shows such plots for three chosen values of r/R_{NL} . (We exclude $n=-2.25$ for economy, but will discuss it further below). To help understand the scales involved in each plot, we also display the values of x/Λ on the upper x -axis. As R_{NL} is a monotonically growing function of time, x/Λ increases from left to right, translating the fact that the spatial resolution relative to the grid increases with time in these plots. We note that in almost all the plots we can identify easily by eye what appears to be a converged value in a finite range of scale (the only exceptions are those of $\bar{\xi}$ in the first panels). In all these cases, a lower cut-off to this converged range is clearly identifiable. As we discussed in the analysis of similar plots in our previous analyses (Joyce et al. 2021; Maleubre et al. 2022), and will see again in detail now, this lower cut-off clearly corresponds to the resolution limit fixed by the ultraviolet cut-offs (Λ and ϵ).

The different estimations of the statistics shown are indicated in the legend and described in the figure caption. Recall that, as detailed in Table 1, the properties of the simulations analysed differ for the two different exponents. While data for $n = -1.5$ correspond to a single realization of each box size, $n = -2.0$ presents data from four different realizations of $N = 1024^3$ boxes and their statistical average.

In the cases in which the rescaled bin is converged following the criterion specified above, in subsection 3.2, at a precision of 1% (i.e. $p = 0.01$), the estimated converged value is indicated as a dashed line and the red shaded region indicates that within 1% of this value. In addition, we add a sub-plot with the dispersion between this value and individual data from direct estimation from all our simulations (including the individual $N = 1024^3$ boxes with $n = -2.0$). This value of 1% is chosen because it is approximately the smallest value of p for which we obtain a significant range of contiguous bins satisfying our convergence criteria. It corresponds to the highest precision (i.e. smallest p) at which we can in practice establish convergence using our data.

The first panel of each figure corresponds to a highly non-linear (small) scale. Although v_r/Hr is not converged at the 1% precision level, the different estimators nevertheless give highly consistent values and appear to show robust convergence albeit at lower precision (of order a few percent), starting from a scale well below Λ . As anticipated in the previous section, the converged value is close to -1 . Further, we see more clearly that this convergence is indeed not

associated with that of $\bar{\xi}$, i.e. at this scale the measured cumulative 2PCF $\bar{\xi}$ approximates very poorly its physical value.

The next (second) panel (of both Fig. 4 and 5) corresponds to the bin around the smallest rescaled separation for which v_r/Hr (in the statistically largest available simulation, using direct estimation) converges (according to our convergence criterion, at the chosen 1% precision level). The lower cut-off to the convergence of v_r/Hr is just slightly below the grid spacing (at about $\Lambda/2$). We see also that $\bar{\xi}$ shows convergence starting from the same scale, so the range of convergence for the pair counting estimator using $\bar{\xi} = 0$, i.e. assuming self-similarity of $\bar{\xi}$, is accurate in a similar range. Looking at the lower sub-panels in the plots of v_r/Hr , we see that the convergence of the direct estimators in the individual $N = 1024^3$ simulations is degraded at slightly larger scales, just above Λ for $n = -1.5$ and slightly below for $n = -2.0$. These are simply finite N (at a fixed Λ) noise in the estimators, as the associated fluctuations disappear in the larger ($N = 4096^3$) simulation for $n = -1.5$ but also when the four $N = 1024^3$ simulations are combined for $n = -2$.

The third panel of both figures shows a considerably larger scale, in the weakly non-linear regime, which have a lower cut-off to convergence (at the 1% level) a few times larger than the grid spacing. In this case, for $n = -1.5$, there is no visible evidence for the finite N effects seen in the previous bin. On the contrary, for $n = -2.0$, we observe much poorer convergence of v_r/Hr both in the direct estimations (lower sub-panel) and in the pair counting estimator (solid lines in main panel). Further, we see now an offset from the estimated converged value that is a systematic shift rather than a random noise, and even in the average over the four simulations, a break from convergence is detected within the range of scale probed. The cancellation (or at least partial cancellation) of these systematic offsets when the realizations are averaged indicates that this is due to significant differences in the initial power at larger scales due to the finite sampling of modes. On the other hand, the observed break from convergence at large scales (in the average) can be attributed to finite box size effects arising from the missing power in modes below the fundamental of the simulation box, finite L , and no longer due to a finite N at fixed Λ as before. These same tendencies are present, but even much more pronounced for $n = -2.25$ (data not shown). Indeed, in this case the lower and upper cut-offs to convergence below the few percent level are no longer clearly separable from one another in almost all bins. For this reason, we do not use the $n = -2.25$ below in our quantitative assessment of resolution limits.

4.1.4 Resolution as a function of time

Applying the analysis detailed above to all bins, we can deduce the comoving scales which are resolved (i.e. self-similar) at each given time, for each of the statistics and estimators we have calculated.

Fig. 6 shows the comoving separation, in units of the grid spacing, of the resolved bins at the 1% (upper two panels) and 5% (lower two panels) precision levels, i.e. of the bins found to be converged according to the criteria described in subsection 3.2 for $p = 0.01$ and $p = 0.05$. The points in the left panels are for the mean pairwise velocity direct estimate using the $N = 4096^3$ simulation for $n = -1.5$ and the average over the four $N = 1024^3$ simulations for $n = -2$. The right panels show the cumulative 2PCF, using the same simulations.

The resolution ranges for $\bar{\xi}$ (in the right panels) can be taken essentially to be those for the mean pairwise velocity estimated from pair conservation and imposing the additional constraint that $\bar{\xi}$ is resolved, i.e. $\bar{\xi} = 0$, because $\xi(r)$ is always resolved starting from a significantly smaller scale than for $\bar{\xi}$ as can be seen in the right panels of Fig. 4 and 5. This is just a simple consequence of the fact that $\bar{\xi}$,

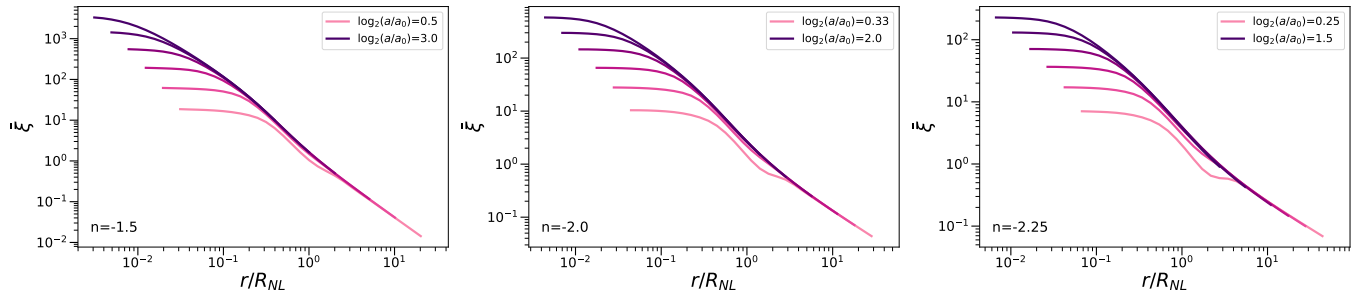


Figure 3. Cumulative 2PCF as a function of rescaled length r/R_{NL} at same times as in Fig. 2. Simulations correspond to $n = -1.5$, $n = -2.0$ and $n = -2.25$, with $N = 4096^3$ in the former exponent and the average over four $N = 1024^3$ for the other two.

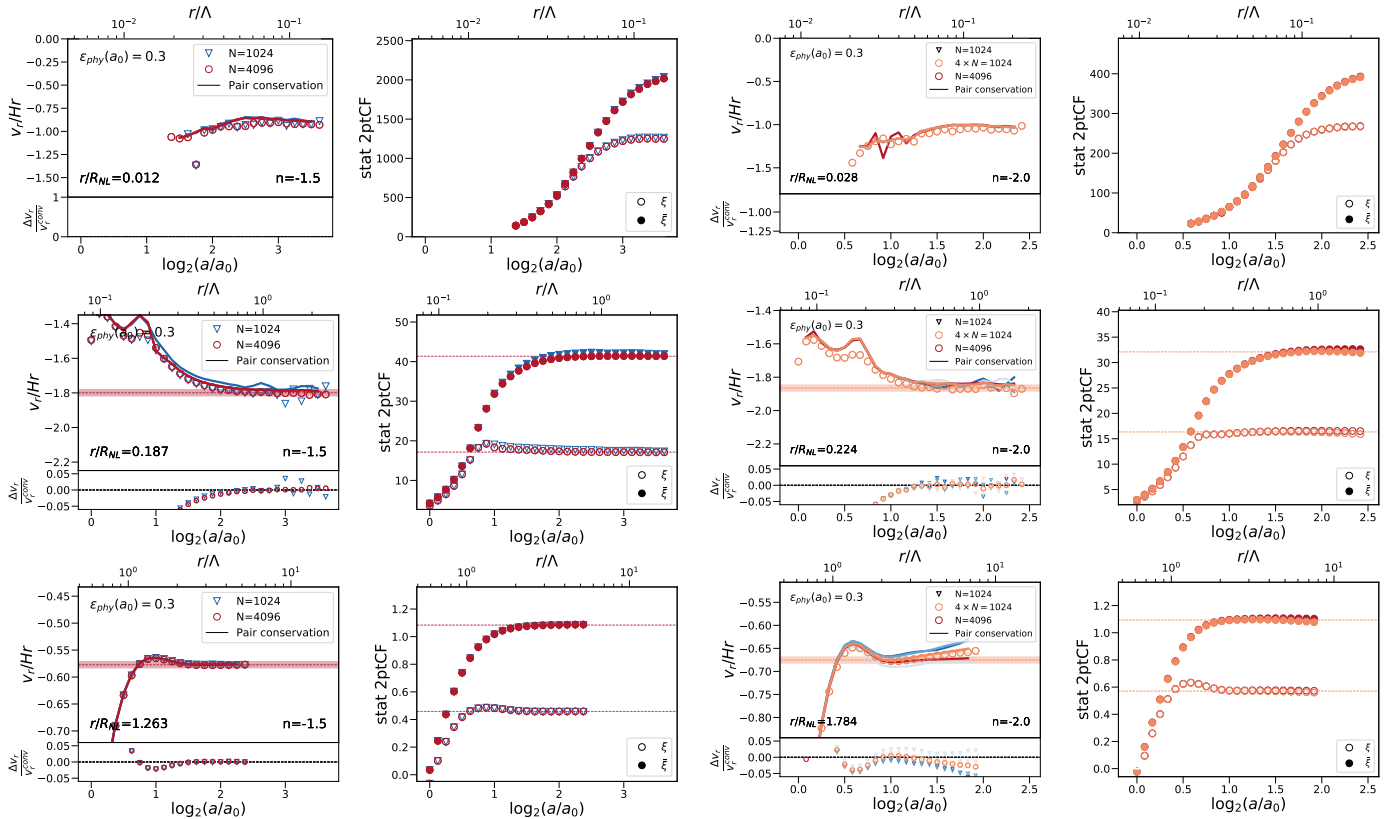


Figure 4. Evolution, for $n = -1.5$ simulations, of v_r/Hr (left panels), and of the 2PCF and cumulative 2PCF (right panels), as a function of logarithmic scale factor $\log_2(a/a_0)$, lower x -axis, and as a function of r/Λ , upper x -axis. Each row correspond to a different bin of rescaled separation r/R_{NL} as labelled. The blue triangular symbol represents the smaller $N = 1024^3$ simulation, while the red circles represent the $N = 4096^3$ simulation. Results obtained using the pair counting estimator are drawn as a continuous line in the appropriate colours. Horizontal red dashed lines indicate the converged value of each of the three statistics, calculated from the largest simulation as described in the text, and the red shaded region indicates that within $\pm 1\%$ of this value. The sub-panels in the plots of v_r/Hr give the dispersion of the results obtained using the direct estimation with respect to the converged value.

by definition, is sensitive (at any given precision level) to $\xi(r)$ over a range of scale below r . It will only therefore be resolved starting from a lower cut-off, below which $\xi(r)$ is resolved over some significant range.

Comparing the upper panels, we see that, as anticipated, the relaxation of the self-similarity constraint extends only very modestly

Figure 5. Same as Fig. 4, but for $n = -2.0$ simulations. There are now four sets of triangular symbols representing the different $N = 1024^3$ simulations (in the sub-panels only), while the orange circles represent the average of the four. Note further that the results for v_r/Hr from the $N = 4096^3$ simulation are all obtained by pair counting only, so that there are no red circles in the left panels.

the resolved regions, for the case of convergence at the 1% level. There are some additional bins that meet the convergence criterion, but most of them are not contiguous with the main converged region and thus do not actually extend the lower limit to resolution (i.e. the scale below which convergence is affected by the unphysical UV scales). In contrast, at 5% precision, there is a very marked difference between the two plots: again as anticipated in our more qualitative analysis above, we see that the resolution of the pairwise velocity now extends down to scales of order the softening length (indicated by the dashed line in each plot). As we will discuss further below, the apparent explanation for this is that the behaviour of the pairwise

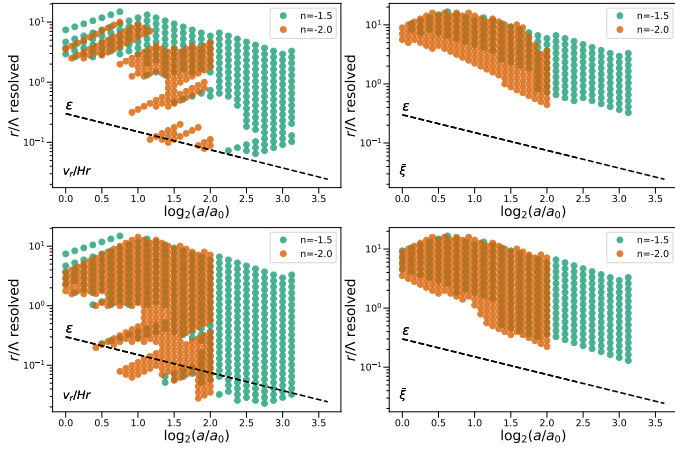


Figure 6. Resolved scales (in units of the initial grid-size, Λ) at 1% (upper row) and 5% (lower row) precision as a function of $\log_2(a/a_0)$. We show results for the spectral indices $n = -1.5$ and $n = -2.0$ (in green and orange, respectively) using the simulations with $N = 4096^3$ for the former and the average of four $N = 1024^3$ simulations for the latter. The left panels show the results for v_r/Hr (direct estimation), while the right shows the results for the *cumulative* 2PCF. The black dashed line shows the evolution of the softening-length ϵ in units of Λ (which is the same in all simulations).

velocity at these small scales — corresponding to stable clustering — remains the same whether the spatial clustering is resolved or not.

4.1.5 Resolution limits extrapolated to LCDM

LCDM models are not scale-free: the linear PS is not a power-law, and there are deviations from EdS power-law scale factor. Nevertheless, the latter deviations are only at very low redshift and the PS, in the range of scales relevant to large scale structure formation in cosmology, can be well approximated as a slowly varying power-law: its logarithmic slope varies roughly between $n = -2.5$ and $n = -1.5$ over two decades in scale. From Fig. 6 we see that the behaviour of the lower cut-off to resolution is quite weakly dependent on n when plotted as a function of a/a_0 . Thus, we can confidently bracket the lower resolution limits (due to the *UV* cut-offs, Λ and ϵ) using the scale-free results. As discussed in our previous analyses, given the physical grid spacing of a LCDM simulation, one can infer a_0 and then obtain a conversion between redshift z and the variable $\log_2(a/a_0)$ which allows an approximate “mapping” of the scale-free results to the LCDM simulation. Taking the tighter bounds obtained for $n = -1.5$, Fig. 7 shows an example of conservative resolution for a simulation with $\Lambda = 0.5h^{-1}\text{Mpc}$. Results are given for a 1% (orange) and 5% (blue) precision in the direct estimation of the pairwise velocity, as plotted in the left panels of Fig. 6. Note that the larger missing scales at 5% simply show that v_r/Hr is converged at much earlier redshifts.

4.1.6 Converged mean pairwise velocities and stable clustering

Having focused on identifying the resolved scales, it is also interesting to look at what can be inferred about the behaviour of the studied statistics, and in particular about their behaviour at asymptotically small scales, where the convergence or deviation from stable clustering is of particular interest.

We show in Fig. 8 the converged values of the normalized pairwise velocity for the three simulated spatial indices. These values correspond to the same analysis used to obtain the left panels in Fig. 6, but

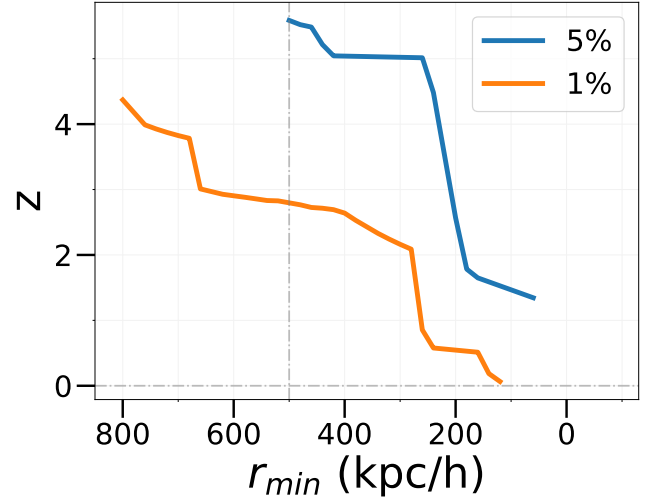


Figure 7. Minimum comoving scale r_{\min} at which v_r/Hr is resolved as a function of redshift, estimated for a standard LCDM cosmology (“Planck 2013”, Planck Collaboration et al. (2014)) in an N -body simulation with a mean-interparticle spacing of $0.5h^{-1}$ Mpc (indicated by dashed vertical line). The orange (blue) line corresponds to the 1% (5%) precision limits, calculated using data from direct estimation as displayed in the left panels of Fig. 6, for the $N = 4096^3$ with $n = -1.5$ simulation.

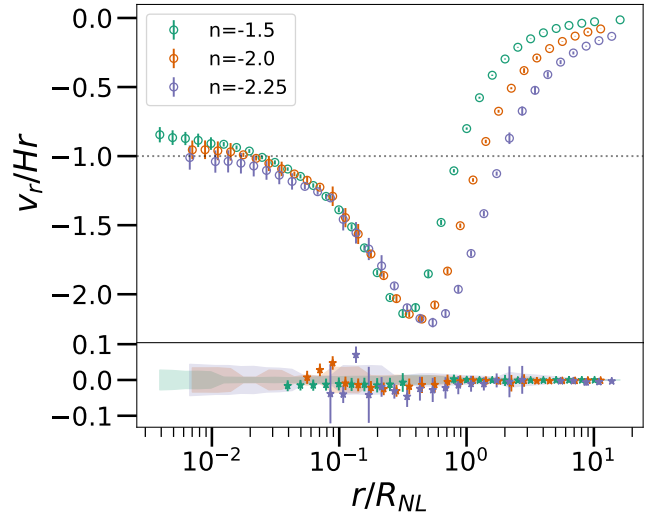


Figure 8. Estimated converged v_r/Hr as a function of rescaled separation, for the three different indicated exponents. In the main plot the same data has been used for the left panels in Fig. 6 i.e. using direct estimation. The converged values are obtained using the 1% and 5% precision criteria, with the error bars estimated as described in the text. The sub-plot shows these same errors as shaded regions; it also shows (star symbols) the relative difference with the converged values obtained using pair counting estimation.

while these show the resolved regions, we now plot the corresponding converged values in each rescaled bin determined by this analysis (i.e. the mean values X_{conv} in the discussion in subsection 3.2). The points plotted are a combination of the values for the bins converged at the 1% level and at the 5% level: we plot X_{conv} for all bins which converge with $p = 0.01$, and then also for the bins which do not converge at $p = 0.01$ but do at $p = 0.05$. We add an indicative estimate of the error on X_{conv} which takes into account the expectation that it

will decrease as the size of the converged window increases:

$$\delta = \pm p \sqrt{\frac{w_{\min}}{w}} \quad (19)$$

where w is the size (in consecutive snapshots) of the converged window (used to calculate X_{conv}) and w_{\min} the smallest window for which Eq. 17 is satisfied, and we have taken here $w_{\min} = 3$. Error bars for the 1% level are smaller than the points, thus where the error bars are visible, the corresponding bins converge only at the 5% level. As could be anticipated, we see that both the accuracy and range of scale measured increases as n does.

We see in this plot that, while there is a clear n -dependence in the shape of the function at larger scales, the behaviour at asymptotically small scales shows a remarkable consistency towards a “universal” stable clustering (bearing in mind that the error bars are only quite rough estimates of the systematic uncertainties due to finite resolution). Posing this to be the correct physical limit also explains why it can be measured quite well even at scales where the physical behaviour of the clustering is not itself resolved: stable clustering is a robust behaviour that it is not spoiled by the discretization of the density field in an N -body simulation.

4.2 Radial pairwise velocities of halos from ROCKSTAR and COMPASO

Leroy et al. (2021) applied the methods we are using here to explore the convergence of the HMF and the 2PCF of halo centres obtained with two different halo finders: a simple FoF algorithm, and ROCKSTAR. This analysis showed, using analysis of a single scale-free simulation with $N = 1024^3$ and $n = -2.0$, that the test of self-similarity clearly shows the much superior convergence of the latter algorithm, revealing very evidently a marked resolution dependence of the measured FoF statistics. We first extend here the comparative analysis to include COMPASO and also make use of our larger simulations and range of exponents to refine the results of Leroy et al. (2021). We then return to the focus of this paper, exploring the convergence of the radial pairwise velocities of halos, comparing it also with that of the 2PCFs.

4.2.1 Halo mass functions

We first show in Fig. 9 the multiplicity function f , as defined in subsection 2.3, as a function of the rescaled mass M/M_{NL} . We refer hereafter to f as the *halo mass function* (HMF). The two left panels correspond to the COMPASO catalogue obtained from the $N = 4096^3$ simulations of $n = -1.5$ (upper) and $n = -2.0$ (lower), while the right panels are for ROCKSTAR catalogue of a single $N = 1024^3$ simulation of the same two exponents. All plots show that the self-similar rescaling appears to apply to a good approximation, especially at late times. The smaller ROCKSTAR boxes show greater deviations at larger rescaled masses, which are simply due to the reduced number of halos in the smaller volume. Also comparing the two indices for each halo finder, we observe that the self-similarity at large rescaled masses show visible deviations at later times for $n = -2.0$, while $n = -1.5$ presents almost no such deviations. This difference mirrors what we observed in the analysis above of the dark matter statistics, and reflects the increasing importance of finite box size as the index of the power spectrum reddens.

Following the same steps as in our analysis of the dark matter statistics, we next study these qualitatively apparent features quantitatively by considering vertical slices in Fig. 9, assessing the self-similarity of the HMF as a function of time in bins of fixed rescaled mass. Fig. 10

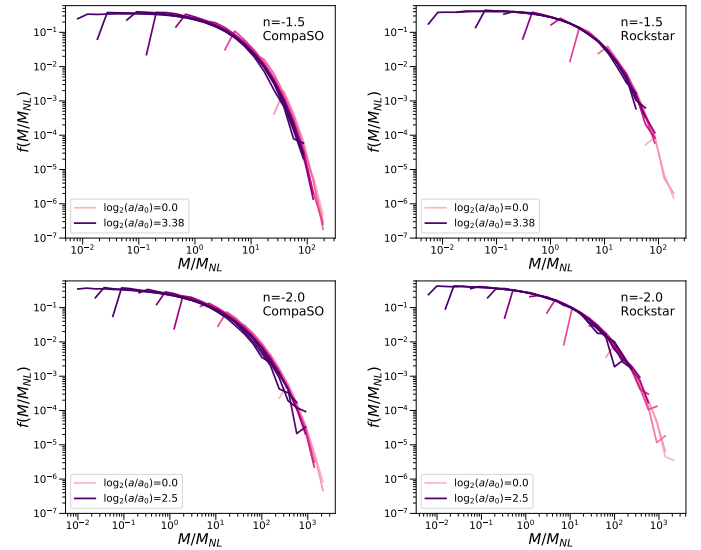


Figure 9. HMF as a function of rescaled mass M/M_{NL} for simulations of spectral index $n = -1.5$ (upper panels) and $n = -2.0$ (lower panels). The left column shows results from COMPASO (after the cleaning procedure detailed in Bose et al. 2022) for the $N = 4096^3$ simulation. The right column shows results from ROCKSTAR for a single $N = 1024^3$ simulation. Self-similar evolution corresponds to the superposition of the curves in each plot. The times shown correspond to every third snapshot $S = 0, 3, 7, \dots$ over the total span of the simulation.

shows the HMF, for $n = -1.5$ (left panels) and $n = -2.0$ (right panels), for the different halo catalogues indicated and three chosen representative rescaled mass bins. We also indicate, on the upper x -axis, the number of particles in a halo (M/m_{part}), where m_{part} is the particle mass of our simulations, on the upper x -axis. As M_{NL} grows as a function of time, the halos populating a given M/M_{NL} bin contain more and more particles as time progresses. We note that the different halo finders have different mass definitions, so in these figures we do not expect agreement in the value of $f(M/M_{\text{NL}})$ but we are interested instead in comparing the time/particle number range in which a convergence to a constant behaviour (i.e. self-similarity) is attained. The horizontal lines in the panels indicate the estimated converged value when such convergence is attained at 1% precision, using exactly the same criteria as detailed in subsection 3.2 (with $p = 0.01$). The uppermost two panels correspond to the smallest rescaled mass at which such convergence is obtained (for at least one of the finders), and the bottom panels to the largest such rescaled mass. This value of 1% is again chosen because it is approximately the smallest value of p for which we obtain a significant range of contiguous bins satisfying our convergence criteria.

Examining these plots, we see several clear trends. ROCKSTAR catalogues show good convergence: the 1% precision level is attained starting from order 10^2 particles, with degrading convergence at larger mass/late time due to smaller box size. COMPASO catalogues show equally good convergence beyond 10^3 particles when the cleaning is performed, while the raw COMPASO catalogues never meet the convergence criteria and show instead a clear monotonic dependence on the resolution. On one hand, the larger number of particles needed for convergence in COMPASO is expected, as the kernel density scale is fixed and does not scale self-similarly (i.e., a new scale is inserted in the problem, which is assumed will affect self-similarity of small objects). On the other hand, the behaviour displayed by the raw COMPASO is very similar to that observed in Leroy et al. (2021) for FoF-selected halos. Thus, the merger-

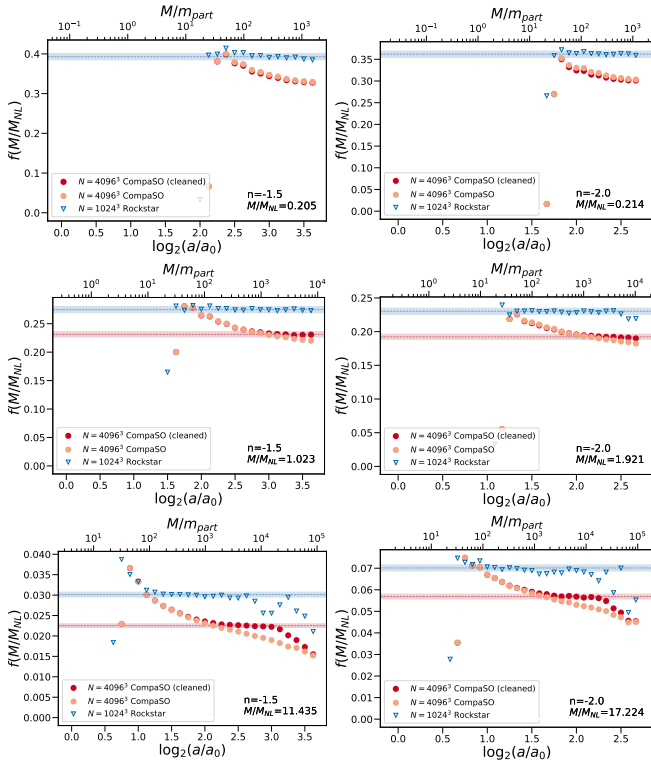


Figure 10. Evolution of the HMF for the index $n = -1.5$ (left column) and $n = -2.0$ (right column) as a function of $\log_2(a/a_0)$, lower x -axis, and halo particle number (M/m_{part}), upper x -axis, for a set of given mass-rescaled bins M/M_{NL} . Blue triangles correspond to ROCKSTAR for a single $N = 1024^3$ simulation, while circles correspond to COMPASO for the $N = 4096^3$ simulation (orange corresponds to results before merger-tree cleaning and red corresponds to results after). Horizontal dashed lines represent the converged value of the HMF, and the shaded regions indicate that within $\pm 1\%$ of this value.

tree based cleaning (discussed in subsection 3.3 above) appears to correct very appropriately the mass of halos, by increasing by the right amount the number of larger halos at each given time to restore the self-similarity.

In the panels in the bottom row, which probe the most massive halos resolved, a clear upper cut-off exists in the convergence in the cleaned COMPASO catalogues at a few times 10^4 particles. Comparing with the plain computer text format latexplain computer text format latexbehaviour seen in the same bin for the smaller ROCKSTAR boxes, which appear to show a down-turn of the data away the converged value at a slightly earlier time, it appears that these deviations can be attributed to finite box size effects. Further tests against larger ROCKSTAR boxes would be desirable to confirm this and exclude any evidence for residual resolution dependence in the cleaned COMPASO, as well as test against self-similarity for the different cleaning parameter values.

Indeed, we note that one of the more general conclusions we can draw is that the self-similarity tests on scale-free models are an excellent tool for testing resolution of halo finders. Furthermore, while we do not claim these tests to be proof of correctness, self-similarity is a necessary evidence for it, and results can be used to place minimal convergence limits to halo finder algorithms.

4.2.2 Pairwise velocities

We now turn to our analysis of the mean pairwise velocities, and the 2PCF, of halo centres. As for the HMF above, the latter extends and also allows comparison with the more limited analysis already reported in Leroy et al. (2021). We have first considered the HMF as we would expect that any other halo statistics, which are generically expected to depend on M/M_{NL} , will be self-similar to a good approximation at a given rescaled r/R_{NL} only if the HMF is also. Amongst other considerations, we will examine below the extent to which this is the case quantitatively for the 2PCF and mean radial pairwise velocity.

Fig. 11 and 12 show, respectively, for the same three rescaled-mass bins in Fig. 10, the 2PCF and mean radial pairwise velocity for halo centres. The latter is calculated directly only, as the pair conservation relation we exploited for the dark matter analysis is not valid for halos. We display results for the cleaned COMPASO catalogues in the $N = 4096^3$ simulations and the indices $n = -1.5$ and $n = -2.0$. We plot the values of the statistic as a function of the rescaled distance r/R_{NL} , and for all redshifts with data in the given bin of rescaled mass. In each plot we have marked by a black vertical line the scale $2r_{\text{vir}}/R_{\text{NL}}$ corresponding to twice the virial radius, r_{vir} , of the corresponding rescaled mass. In addition, the shaded area marks the corresponding scale to the minimum and maximum mass limits on the finite bin. Although COMPASO halos may be separated by less than $2r_{\text{vir}}$ (as they are neither spherical nor have a spatial extent directly determined by r_{vir}) we expect a scale of this order to be an effective lower cut-off to the range in which a physical halo correlation function can be measured.

Fig. 11 and 12 display qualitative behaviour similar to that in the statistics we have analysed previously: both statistics show clear self-similarity propagating in time from larger to smaller scales in time. As anticipated, the scale $2r_{\text{vir}}/R_{\text{NL}}$ does seem to give a good indication of the lower cut-off scale. Perhaps surprisingly, at the latest times self-similarity seems even to extend to separations as small as r_{vir} . Further the plots appear to show, again perhaps surprisingly, that the convergence of v_r is slightly better than that of the 2PCF.

Following again the analysis in the previous sections, to assess more fully and quantify these behaviours, we take vertical slices in Fig. 11 12. As v_r/Hr and ξ are each functions of the two rescaled variables r/R_{NL} and M/M_{NL} , each such plot thus corresponds now to a specific bin of each of these two variables (and self-similarity again to a time independent behaviour of the dimensionless statistics). Limitations of space here impose the choice of a few illustrative values of r/R_{NL} and M/M_{NL} .

In Fig. 13 we show three plots for each of the two statistics, for ROCKSTAR and cleaned COMPASO halo catalogues obtained in the $N = 1024^3$ and $N = 4096^3$ simulations of $n = -1.5$, respectively: the bins correspond to three values of M/M_{NL} over the range in which we obtain satisfaction of our convergence criteria at the 2% level, and for which, as in the previous figures the converged values are indicated by horizontal lines and the precision by the shaded regions. The value of r/R_{NL} in each bin has been chosen to correspond approximately to $2r_{\text{vir}}/R_{\text{NL}}$, which is approximately the smallest scale from which we observe convergence of both statistics (using the same criteria). Just as in the plots for the HMF in Fig. 10, we also plot in the upper x -axis the number of particles in the analysed halos as a function of time. We do not display the results for the raw COMPASO catalogue because this data is almost exactly superimposed on that for the cleaned catalogue (more remarkably for v_r/Hr): differently to what we observed for the HMF, the accuracy of these halo statistics, and indeed their convergence (see below), is insensitive to the

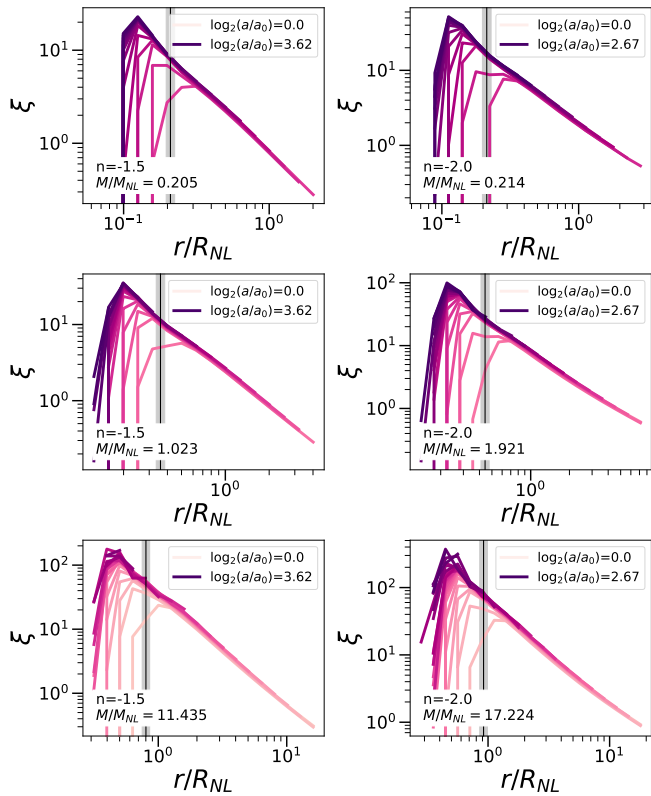


Figure 11. 2PCF as a function of rescaled separation r/R_{NL} , for $n = -1.5$ (left column) and $n = -2.0$ (right column) simulations. The statistic is computed for each bin of rescaled mass M/M_{NL} , showing here those corresponding with Fig. 10. The data corresponds to cleaned COMPASO for the $N = 4096^3$ simulations. Per mass bin, we show all snapshots containing halos in said bin.

associated re-assignment of particles. The value of 2% precision has (like in the corresponding HMF plots above) been chosen because it is approximately the smallest value of p for which we obtain a significant range of contiguous bins satisfying our convergence criteria, corresponding to the highest precision at which we can in practice establish convergence using our data.

As anticipated from Fig. 11 and 12, the convergence of the pairwise velocity (left panels) is indeed significantly better than that of the 2PCF (right panels). Convergence is attained (at a given precision, here 2%) starting from a smaller particle number (i.e. earlier in time). This difference becomes more pronounced in the largest mass bin, as clearly illustrated here in the chosen bin (bottom plots in the figure) in which the 2PCF alone fails to meet the convergence criteria. We believe the explanation for this comes from the very different dependencies of the two statistics on the rescaled mass. Comparing the converged values of the two statistics in the different mass bins in Fig. 13, we see that the pairwise velocity is only very weakly dependent on the mass compared to the 2PCF: the former varies by only 20%, while the latter changes by a factor of 5 (as the mass itself varies by a factor of 50). Errors in the mass assignment of the halos selected in a given mass bin will thus feed through to give a much larger error in the 2PCF.

Examining further the lower bounds to convergence, we observe that the ROCKSTAR data converges on small scales at fewer particles per halo than the COMPASO, while both perform equivalently at larger scales. This is clearest in the lowest mass bin, extending to the larger

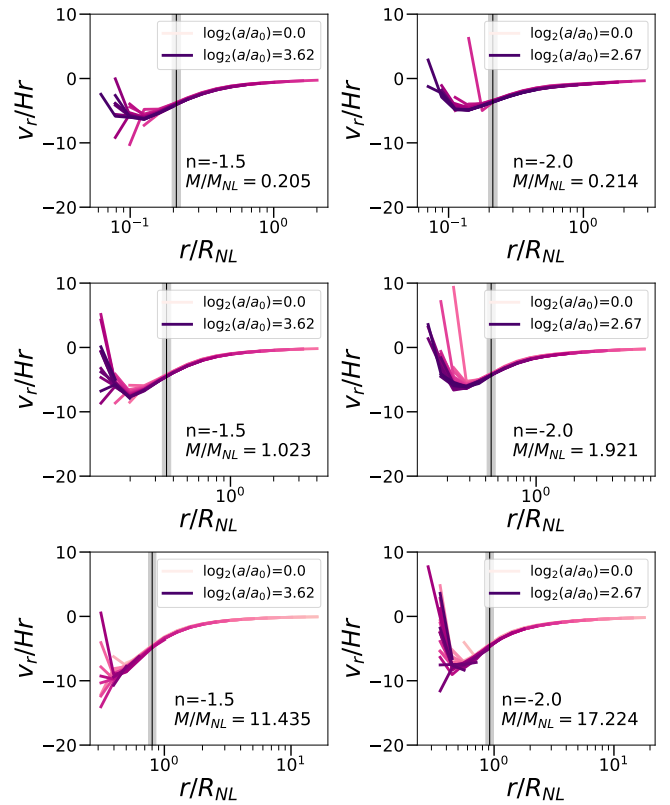


Figure 12. Same as Fig. 11 but for the estimation of v_r/Hr .

mass bins, albeit somewhat obscured by the relative noisiness at larger scales of the ROCKSTAR data (due to smaller box size).

4.2.3 Resolution limits for halo statistics in scale-free and LCDM-type simulations

As we have discussed, the lower cut-offs to convergence for the halo statistics we have analysed can be stated as cut-offs on the number of particles per halo, and in the case of the correlation functions (which depend also on separation) also in terms of a cut-off on separation in units of the virial radius. Further, in the data shown above we have seen that in practice the requirement on particle number, for a given halo finder, seems not to depend significantly on the mass bin for the HMF or the pairwise velocity at a given scale, at least for the approximately fixed separations (in units of virial radius) which we examined.

Fig. 14 presents a more complete view of the data to test whether these behaviours are really valid in general: for $n = -1.5$ (upper panels) and $n = -2$ (lower panels), the leftmost panel shows in each case the lower cut-off to convergence expressed in particles per halo for the HMF as a function of the rescaled mass, while the other two panels show, for the pairwise velocity and 2PCF respectively, the analogous quantity as a function of separation in units of r_{vir} , and for different bins of rescaled mass. In each plot, the two sets of curves shown correspond to the two indicated halo finders (full line/circles to cleaned COMPASO and dotted lines/stars to ROCKSTAR), and each of the curves (or points) to different mass bins M/M_{NL} . The dashed-thick lines correspond to best (least-squares) fits of a linear dependence on $r/r_{vir} - M/M_{NL}$ for the HMF case – to the data (for each of the halo-finders separately). All results correspond

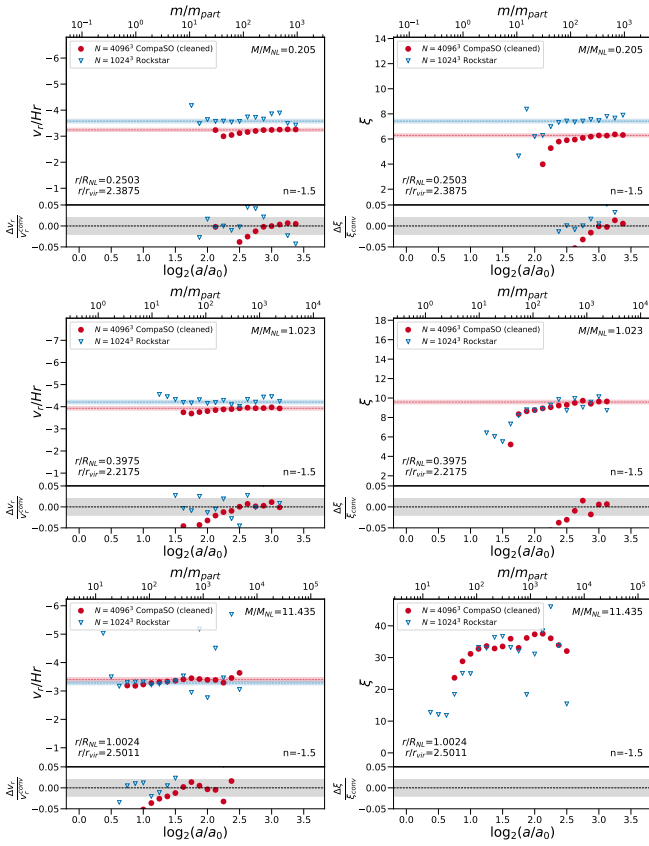


Figure 13. Evolution, for $n = -1.5$ simulations, of v_r/Hr (left column) and the 2PCF (right column) as a function of $\log_2(a/a_0)$, lower x -axis, and number of particles in the halo, upper x -axis. Each plot shows the scale closer to $\sim 2r_{\text{vir}}$ for each mass-bin on Fig. 9. Blue triangles correspond to ROCKSTAR for a single $N = 1024^3$ simulation, while red circles correspond to cleaned COMPASO for the $N = 4096^3$ simulation. Horizontal red dashed lines represent the convergence value of v_r/Hr and 2PCF, and the shaded regions indicate that within $\pm 2\%$ of this value. The lower panel of each plot indicates the dispersion of the direct measurement of the statistic with respect to its converged value, while the shaded region covers the imposed $\pm 2\%$ precision.

to our best reported precision: 1% for the HMF and 2% for the 2PCF and pairwise velocity.

The plots for v_r show that the anticipated behaviours indeed hold: the bounds for the different mass-bins collapse approximately onto a single line and can thus be well approximated as a bound on the number of particles per halo as a function of r/r_{vir} exclusively. On the other hand, the column plotting the ξ data shows that, although the dependence on M/M_{NL} is weak for the converged values, the quality of convergence for large mass-bins (and large scales) is significantly reduced with respect to the former statistic.

The behaviours also confirm and further quantify the trends we observed in subsection 4.2.2. In particular, we see that the number of particles per halo required for a self-similar behaviour is, for each of the two statistics, indeed higher for COMPASO than ROCKSTAR at small scales, but this difference disappears progressively as we go to larger scales, where both halo finders perform similarly. We also see further quantified the better convergence of v_r compared to ξ . Finally, we note that the actual number of particles per halo required to meet the convergence criteria for these two statistics are in fact considerably smaller than those required for the HMF. Although convergence for the latter is established at a 1% and the 2-pt statistics are only converged at 2% level, relaxing the precision limits for the

HMF only changes very slightly the required particle numbers. This is explained in the same way as we explained the relative quality of the convergence of v_r and the 2PCF: the HMF is itself a much stronger function of rescaled mass than the 2PCF (and a fortiori than v_r). For example, comparing the second to third rows of Fig. 10, we see that the HMF changes by a factor of 10, while in Fig. 13 (as discussed above) we see that the 2PCF varies by a factor of 3 and the mean pairwise velocity only by 20%. Thus, to obtain a 2% error in v_r and ξ we can tolerate a much larger error in the mass function. It is for the same reason that v_r (and ξ in some range) show no significant sensitivity to the cleaning of the COMPASO catalogues, as these correspond (as seen above) to relatively small changes to the mass assigned to halos.

Finally, we see that the two sets of plots, for $n = -1.5$ and $n = -2.0$, differ only very marginally. Further, they are formulated in terms of mass and length units (M_{NL} and r_{vir}) that are also clearly defined not just in scale-free cosmologies but in any cosmology. Given this, it is very reasonable to take these resolution bounds to be appropriate for any cosmology, like LCDM, in the range in which structures are seeded by a linear power spectrum with a close to power law behaviour and comparable exponents to these. One caveat is that the scale-free models are EdS cosmologies, so more caution should be used when adapting the bounds at $z \approx 0$ where deviations from EdS become significant. Nevertheless, it seems unlikely that these effects, arising essentially from the resolution limits on identification of halos, would have significant sensitivity to the background cosmology.

5 CONCLUSIONS

The analysis we have reported here is an extension of that in a set of papers (Joyce et al. 2021; Leroy et al. 2021; Garrison et al. 2021a; Garrison et al. 2021c; Maleubre et al. 2022), which have shown the usefulness of self-similarity and scale-free cosmologies in quantifying resolution of cosmological N -body simulations. Our focus here has been on the radial component of the pairwise velocity, both in the full matter field and for halos selected using the ROCKSTAR and COMPASO catalogues. We have also extended, as a complement and for comparison, the analysis of the 2PCF of the matter field (previously studied in Joyce et al. 2021; Garrison et al. 2021a) and of the HMF and 2PCF for halos (previously studied in Leroy et al. 2021). Compared to these previous studies which used a single power law ($n = -2.0$) and simulations of a single size ($N = 1024^3$), as in Maleubre et al. (2022) we have considered a set of both different power laws and different box sizes. Unsurprisingly, we have found that the same methods indeed allow us to quantify the evolution of resolution at small scales of the mean pairwise velocity, and further confirm the high levels of accuracy attained by the ABACUS code also in its determination of correlations in the velocity field. Further, in line with Leroy et al. (2021), we find that self-similarity tests are indeed an excellent tool to assess the performance of different halo finders, as shown by their capacity to detect the subtle differences resulting from the cleaning of the COMPASO catalogues.

Our exploitation here of simulations of different sizes, of several realizations, and of scale-free models with different exponents has allowed us not only to improve some of the results in this previous work (notably concerning halos) but has also been essential to allow us to extend the method to a velocity statistic. This is the case because it is crucial for an accurate determination of the precision of convergence to be able to separate very clearly the effects of discretization at small scale from both the noise and systematic effects at large scales

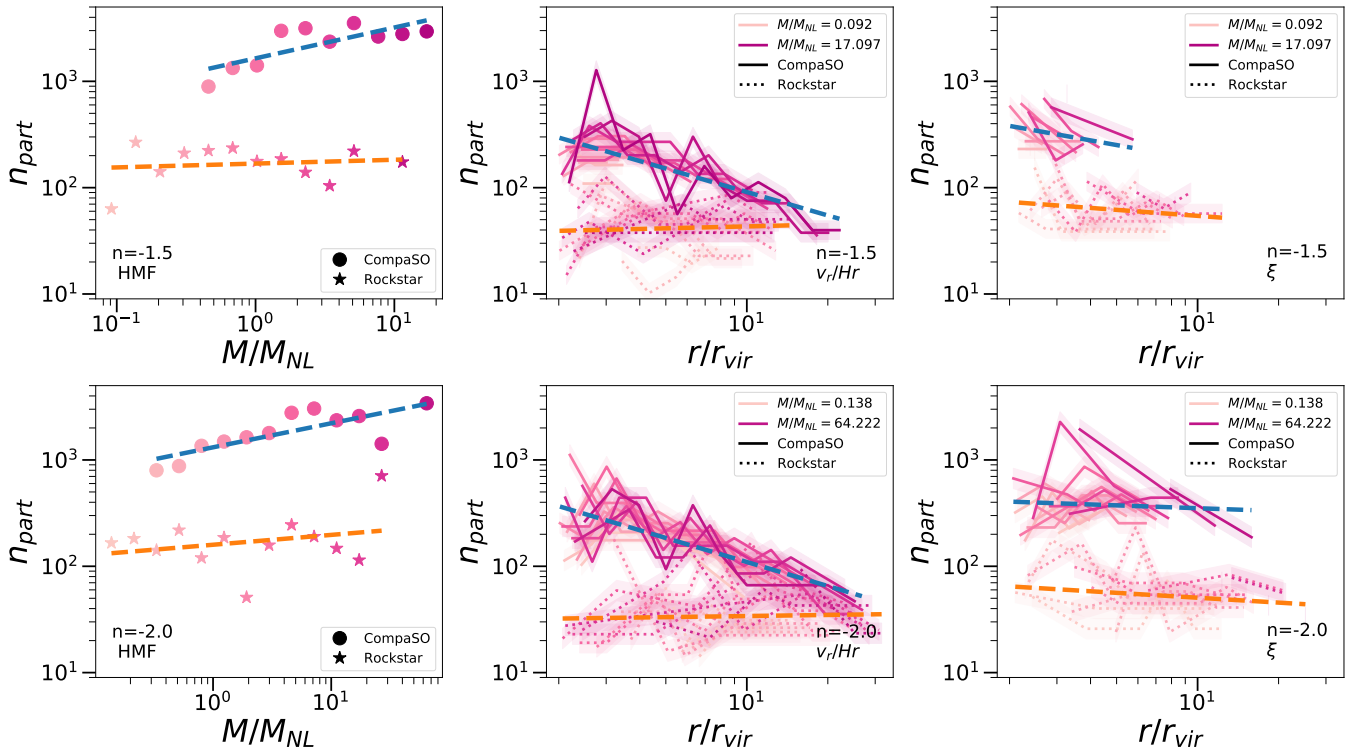


Figure 14. Minimum number of particles needed, at each M/M_{NL} bin, for convergence of: HMF (left panel), mean pairwise velocity (middle panel) and 2PCF (right panel), with the last two computed in addition at different r/r_{vir} bins. All results correspond to our best reported precision: 1% for HMF and 2% for pairwise velocity and 2PCF. Solid lines/circles correspond to cleaned COMPASO while dashed lines/stars correspond to ROCKSTAR. The blue and orange dashed lines are the least squares best fit of all mass-bin data. The axes are the same in all plots to facilitate comparison.

due to the finite box size. For the pairwise velocity statistics, which are more sensitive than the 2PCF to these effects, the comparison of different (and larger) box sizes and different exponents turns out to be essential to disentangle clearly the different effects. We have also exploited the two different estimators of the statistic — directly from the velocities or indirectly by pair-counting — to identify noise due to finite size effects. The comparison of different exponents has allowed us also to see how the range of converged scales markedly degrades due to finite size effects as n decreases, and in practice our $n = -2.25$ simulations are not useful for placing precision limits at the 1% level. Further, we argue that our results for the evolution of small scale resolution can be extrapolated to LCDM type models, as they are, when suitably expressed, very weakly dependent on scale-free index n (which have been chosen to probe the relevant range). The same is not true of box size effects, which are strongly n dependent, and indeed we do not attempt to make an extrapolation for these.

For the pairwise velocity of the dark matter, we have found that we can determine the evolution of lower cut-off to resolution at the 1% level. It is approximately equal to the corresponding cut-off for the *cumulative* 2PCF, which converges at the same precision level varying from a few times the grid spacing at early times to slightly below this scale at late times. This is a few times larger than the scale at which the 2PCF itself attains the same precision (Joyce et al. 2021; Garrison et al. 2021a). This reflects the coupling of the velocity correlation at a given scale to the clustering at smaller scales (as expressed through the integral $\bar{\xi}$ in the self-similar limit). On the other hand, at 5% precision we have obtained resolution extending down to scales of order the softening ϵ , where even the 2PCF is far from its converged value (Joyce et al. 2021; Garrison et al. 2021a). In the

corresponding range of scale $v_r/Hr \approx -1$, i.e. the result is consistent with the so-called stable clustering hypothesis in which non-linear structures become stationary in physical coordinates (Peebles 1974). The conclusion that clustering may indeed tend to this behaviour at asymptotically small scales is consistent with an early analysis (with much smaller simulations, $N \sim 10^6$) of the question using pairwise velocities by Jain (1997) (estimated by pair-counting), and also with results for the shape of the power spectrum at large k reported in Maleubre et al. (2022). In this hypothesis, the fact that resolution extends to such small scales for v_r/Hr is simply due to the fact that the stable behaviour is not spoiled by the discretization of the matter field, and persists even if the clustering is very different to that in the continuum model.

For the halo statistics, extending the analysis of Leroy et al. (2021), we have been able to use our data to establish resolution limits at the 1% precision level for the HMF, and at the 2% level for the 2PCF and pairwise velocity in both the ROCKSTAR catalogues and the COMPASO catalogues, provided the cleaned version described in Bose et al. (2022) is used for the HMF. As in Leroy et al. (2021) we express the lower limits to resolution for the HMF as a lower limit on the number of particles, which turns out to be roughly independent of the mass. For the pairwise velocity and 2PCF, which are also functions of separation, we find that the lower bounds on the number of particles are, to a good approximation, independent of mass when plotted as a function of separation in units of the virial radius (corresponding to the given mass).

Plotting the inferred lower bounds on particle numbers for each of the three statistics, for $n = -1.5$ and $n = -2$ simulations, shows that the results show no significant dependence on n and thus can be confidently adopted to LCDM-like simulations. At the 1% level,

ROCKSTAR is not able to resolve the HMF below $\sim 100\text{--}200$ particles, the cleaned version of COMPASO breaks self-similarity below ~ 1000 particles, and its raw version never achieves this convergence at the same precision. For the 2PCF and pairwise velocities, the 2% precision level is attained with significantly smaller particle numbers than the previous statistic, with the latter requiring the least. For these, the effects of cleaning COMPASO are less significant, as the dependence on mass-bin is suppressed. At small scales, ROCKSTAR exhibits self-similarity starting at a smaller particle number than COMPASO, plausibly explained by the introduction of a fixed kernel density scale in the latter, which the authors assume will certainly affect self-similarity of small objects. This difference decreases as the separation increases and disappears at $(10 - 20)r_{\text{vir}}$.

With respect to the preparation of theoretical predictions for forthcoming surveys, and specifically for redshift space distortions, our analysis of the pairwise velocity gives only an indication of the resolution limits at small scales in N -body simulations. It would be straightforward to extend our analysis to additional statistics used in this context e.g. PDFs of the pairwise velocity and their moments (see references in introduction). Further, to attain a quantification of bounds for the typically cited target 1% level would require slightly more data sets than what we have used here — either slightly larger simulations, or a couple of realizations of the same size as our largest simulations here.

We conclude with some comments on other possible further developments of this work. Our analysis has confirmed the finding of Leroy et al. (2021) that self-similarity is a powerful tool to put halo algorithms to the test and compare their resolution. It would be interesting to explore in particular whether the COMPASO algorithm can be further modified in order to improve its resolution at low halo mass, while maintaining its computational speed. Our analysis of the mean pairwise velocities in the dark matter field (cf. Fig. 8) shows an apparently universal shape below the scale of maximal infall, and going asymptotically to stable clustering. It would be interesting to compare these results with those in LCDM, making use of the resolution limits we have determined here, to assess whether we indeed find the same behaviour. To establish the evidence for stable clustering at asymptotically small scales, a fuller comparative joint analysis of the 2PCF, PS, and pairwise velocity itself should be performed. Finally, we note that the results we have derived here can be exploited to study in a very controlled way the bias of both the 2PCF and the pairwise velocities of the halos relative to the dark matter field, as a function of mass.

ACKNOWLEDGEMENTS

S.M. thanks Sownak Bose for guidance and technical support with the halo merger tree code for ABACUSSUMMIT, used to *clean* the COMPASO catalogue of the scale-free simulations used in this paper. She also thanks the Institute for Theory and Computation (ITC) and the Flatiron Institute for hosting her in early 2022, and acknowledges the Fondation CFM pour la Recherche and the German Academic Exchange Service (DAAD) for financial support. S.M. and M.J. thank Pauline Zarrouk for useful discussions.

D.J.E. is supported by U.S. Department of Energy grant, now DE-SC0007881, NASA ROSES grant 12-EUCLID12-0004, and as a Simons Foundation Investigator.

This research used resources of the Oak Ridge Leadership Computing Facility at the Oak Ridge National Laboratory, which is supported by the Office of Science of the U.S. Department of Energy under Contract No. DE-AC05-00OR22725. The ABACUSSUMMIT simu-

lations have been supported by OLCF projects AST135 and AST145, the latter through the U.S. Department of Energy ALCC program.

DATA AVAILABILITY

Data access for the simulations part of ABACUSSUMMIT is available through OLCF's Constellation portal. The persistent DOI describing the data release is [10.13139/OLCF/1811689](https://doi.org/10.13139/OLCF/1811689). Instructions for accessing the data are given at <https://abacussummit.readthedocs.io/en/latest/data-access.html>.

Data corresponding to the smaller simulations as well as the derived data generated in this research will be shared on reasonable request to the corresponding author.

REFERENCES

- Behroozi P. S., Wechsler R. H., Wu H.-Y., 2013, *ApJ*, **762**, 109
 Bibiano A., Croton D. J., 2017, *MNRAS*, **467**, 1386
 Bose S., Eisenstein D. J., Hadzhiyska B., Garrison L. H., Yuan S., 2022, *MNRAS*, **512**, 837
 Brando G., Koyama K., Wands D., 2021, *JCAP*, 2021, 013
 Clifton T., Ferreira P. G., Padilla A., Skordis C., 2012, *Physics Reports*, **513**, 1
 Cole S., et al., 2005, *MNRAS*, **362**, 505
 DESI Collaboration et al., 2016, arXiv e-prints, p. arXiv:1611.00036
 Davis M., Peebles P. J. E., 1977, *ApJS*, **34**, 425
 Eisenstein D. J., et al., 2005, *ApJ*, **633**, 560
 Euclid Collaboration et al., 2019, *MNRAS*, **484**, 5509
 Garrison L. H., Eisenstein D. J., Ferrer D., Metchnik M. V., Pinto P. A., 2016, *MNRAS*, **461**, 4125
 Garrison L. H., Eisenstein D. J., Pinto P. A., 2019, *MNRAS*, **485**, 3370
 Garrison L. H., Joyce M., Eisenstein D. J., 2021a, *MNRAS*, **504**, 3550
 Garrison L. H., Eisenstein D. J., Ferrer D., Maksimova N. A., Pinto P. A., 2021b, *MNRAS*, **508**, 575
 Garrison L. H., Abel T., Eisenstein D. J., 2021c, *MNRAS*, **509**, 2281
 Gronke M., Llinares C., Mota D. F., Winther H. A., 2015, *MNRAS*, **449**, 2837
 Grove C., et al., 2022, *MNRAS*, **515**, 1854
 Hadzhiyska B., Eisenstein D., Bose S., Garrison L. H., Maksimova N., 2022, *MNRAS*, **509**, 501
 Heitmann K., et al., 2008, *Computational Science and Discovery*, **1**, 015003
 Hellwing W. A., Barreira A., Frenk C. S., Li B., Cole S., 2014, *Phys. Rev. Lett.*, **112**, 221102
 Jackson J. C., 1972, *MNRAS*, **156**, 1P
 Jaffe A. H., et al., 2001, *Phys. Rev. Lett.*, **86**, 3475
 Jain B., 1997, *MNRAS*, **287**, 687
 Jenkins A., Frenk C. S., White S. D. M., Colberg J. M., Cole S., Evrard A. E., Couchman H. M. P., Yoshida N., 2001, *MNRAS*, **321**, 372
 Joyce M., Marcos B., 2007, *Phys. Rev. D*, **76**, 103505
 Joyce M., Garrison L., Eisenstein D., 2021, *MNRAS*, **501**, 5051
 Kaiser N., 1987, *MNRAS*, **227**, 1
 Knebe A., et al., 2011, *MNRAS*, **415**, 2293
 Laureijs R., et al., 2011, arXiv e-prints, p. arXiv:1110.3193
 Leroy M., Garrison L., Eisenstein D., Joyce M., Maleubre S., 2021, *MNRAS*, **501**, 5064
 Maksimova N. A., Garrison L. H., Eisenstein D. J., Hadzhiyska B., Bose S., Satterthwaite T. P., 2021, *MNRAS*, **508**, 4017
 Maleubre S., Eisenstein D., Garrison L. H., Joyce M., 2022, *MNRAS*, **512**, 1829
 Nityananda R., Padmanabhan T., 1994, *MNRAS*, **271**, 976
 Peebles P. J. E., 1974, *ApJ*, **189**, L51
 Perenon L., Bel J., Maartens R., de la Cruz-Dombriz A., 2019, *JCAP*, 2019, 020
 Perlmutter S., et al., 1997, *ApJ*, **483**, 565

- Planck Collaboration et al., 2014, *A&A*, **571**, A16
- Press W. H., Schechter P., 1974, *ApJ*, **187**, 425
- Pryke C., Halverson N. W., Leitch E. M., Kovac J., Carlstrom J. E., Holzzapfel W. L., Dragovan M., 2002, *ApJ*, **568**, 46
- Riess A. G., et al., 1998, *The Astronomical Journal*, 116, 1009
- Schneider A., et al., 2016, *JCAP*, 2016, 047
- Sinha M., Garrison L. H., 2019, in Majumdar A., Arora R., eds, *Software Challenges to Exascale Computing*. Springer Singapore, Singapore, pp 3–20, https://doi.org/10.1007/978-981-13-7729-7_1
- Sinha M., Garrison L. H., 2020, *MNRAS*, **491**, 3022
- Tinker J., Kravtsov A. V., Klypin A., Abazajian K., Warren M., Yepes G., Gottlöber S., Holz D. E., 2008, *ApJ*, **688**, 709
- Valogiannis G., Bean R., Aviles A., 2020, *JCAP*, **2020**, 055

This paper has been typeset from a \TeX/L\AA\TeX file prepared by the author.